Journal of Materials Chemistry A

Accepted Manuscript

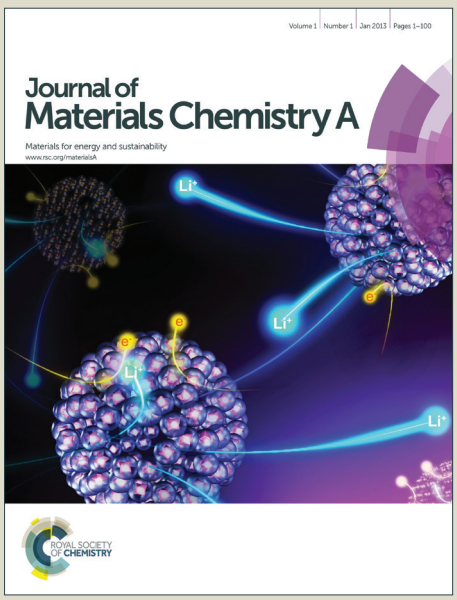

ROYAL SOCIETY OF CHEMISTRY

www.rsc.org/materialsA

Uniformly Dispersed Self-Assembled Growth of Sb_2O_3/Sb@Graphene Nanocomposites on 3D Carbon Sheet Network for High Na-Storage and Excellent Stability

N. Li, S. Liao, Y. Sun, H. W. Song and C. X. Wang*

State key laboratory of optoelectronic materials and technologies, School of Physics Science and Engineering, Sun Yat-sen (Zhongshan) University, Guangzhou 510275, People's Republic of China

Abstract

The large volume change was the root of a series of knotty problems involved in alloy-type anodes, such as pulverization, exfoliation and the resulted capacity decay. Therefore, the solutions for the problems caused by large volume change in sodium ion batteries (SIBs) anodes were in urgent need. Herein, we report on a novel route for the encapsulation of Sb_2O_3/Sb nanoparticles (Sb_2O_3/Sb-NPs) within graphene shell nanostructure (Sb_2O_3/Sb@graphene) *via* the microwave plasma irradiation of $Sb(CH_3COO)_3$ and the following graphene growth procedure. The designed structure, Sb_2O_3/Sb@graphene NPs anchored on the carbon sheet networks (CSNs), provides an ultra-thin, flexible graphene shell to accommodate the volume changes of Sb_2O_3/Sb, and thus demonstrates excellent cycling stability (92.7% retained after 275 cycles), long cycle life (more than 330 cycles) and good rate capability (220.8 $mAhg^{-1}$ even at 5A/g). The stability could be compared to that of the commercial graphite in lithium ion battery.

Keywords: Sb_2O_3/Sb; carbon sheet network; graphene; sodium ion battery.

* Correspondence and requests for materials should be addressed to C.X.W. e-mail: wchengx@mail.sysu.edu.cn

Introduction

Recently, researches on sodium ion battery (SIB) have been resurrected[1-3], considering the greater natural abundance and a more uniform distribution of Na resource compared to Li[4, 5]. The key impact for the widespread application of SIB is the development of stable and high capacity electrode material with fast charge/discharge rate capability[6]. Unfortunately, the stable capacity was generally limited by the large volume change, structural pulverization [7-11] and unstable solid electrolyte interphase (SEI) film[7, 9], and the rate capability was often kept down by the slow sodium ion diffusion kinetics.

As promising anodes of SIB, antimony (Sb)/antimony oxide have attracted attention owing to their high theoretical capacity of 660 mAh g^{-1} (upon full sodiation Sb-3Na), 1220 $mAhg^{-1}$ (Sb_2O_4-14Na) and 1102 $mAhg^{-1}$(Sb_2O_3-12Na). So far, mainly three kinds of designs were studied, including pure Sb nanostructures (mono-disperse Sb nanocrystals [12], bulk Sb [13]); Sb-carbon composites (Sb/C fibers[11], Sb embedded carbon[14], milled Sb/CNT nano composites[15], Sb/graphene[16], Sb hollow nanospheres[17]) and Sb-based alloys (Mo_3Sb_7[18], SnSb[19], Sb/Cu_2Sb[20], Sb oxides (Sb_2O_3 nanowire[21], Sb_2O_4 film[22]). As for pure Sb active materials, bulk Sb[13] could achieve 160 cycles with a stable capacity of 576 mAh g^{-1} at current rate of C/2 by using an electrolyte with a fluoroethylene carbonate (FEC) additive. The FEC additive has been commonly used to improve the stability of the solid electrolyte interface (SEI) film. However, the stable cycling will degrade fast in 20 cycles without the FEC additive at C/2, let alone at larger current rate. Long term and stable cycling performance was accomplished by the Sb@C fibers [11] (>300 cycles) with a capacity decay of 0.06% per cycle. Both cycling stability and rate capability were improved using an FEC-free electrolyte (405 mAh g^{-1} at 0.1A g^{-1}, 104 mAh g^{-1}at 5 A g^{-1}). Actually, the

conductivity of hard carbon fiber was relatively poor, which was unfavorable for the transmission of electron and Na^+. The hard carbon fiber mainly confined the volume expansion of Sb nanoparticles. Overall, the cycling stability and high rate capability are closely related to the electrochemical stability and electric conductivity of anodes. If the very light weight superconductive graphene was applied to buffer the volume expansion and enhance the conductivity of the composite, the cycling stability and high rate capability could be improved a lot.

Herein, we design a novel three dimensional foam-like Sb-carbon network nanostructures, in which Sb/Sb_2O_3 particles are prepared into nano-size; carbon sheets network (CNS) acted as skeletons of the 3D composites to support Sb/Sb_2O_3 nanoparticles; especially, graphene shells were coated on the dispersive Sb/Sb_2O_3 nanoparticles to accommodate their volume change and enhance the conductivity of the composites. The key point about this design is the controlling of graphene layers, as Na^+ hardly passes through a highly oriented graphite layer. The composites were synthesized through a simple and fast chemically vapor deposition process. As shown in Scheme1, nano-sized Sb particles were encapsulated in graphene shells (Sb@GS), which were homogeneously distributed on carbon sheets network (Sb@GS-CSN). The Sb@GS-CSNs provides large efficient surface area and crisscrossed transport pathways for both ions and electrons, which contributes a lot to its good electrochemical performance at either low or high current density: cycle lives of more than 275 times with a capacity loss of 7.3%; 523 mAh g^{-1} at 100 mA g^{-1} and 223 mAh g^{-1} at even 5 A g^{-1}.

Results and Discussion

The experiment was carried out through a Microwave plasma enhanced chemical vapor deposition (MPECVD) system. A thick layer of the precursor powder

($Sb(CH_3COO)_3$) was homogeneously spread on a Al_2O_3 ceramic wafer (Figure 1a). The synthesis procedure mainly includes three steps: (1) the decomposition of antimony acetate (150 ℃ -400 ℃). $Sb(CH_3COO)_3$ decomposed ($Sb(CH_3COO)_3 \rightarrow Sb_2O_3+C(-COOH) + H_2O+CO_x$) when the temperature was above 150℃. As illustrated in Figure 1b, carbon bubbles were sharply blown by the resulted gases and then immediately burst, leaving interconnected carbon sheet networks anchored with dense Sb_2O_3 nanoparticles (Sb_2O_3-CSNs) (Figure S1). (2) Rapid heating process accompanied by the partly reduction of Sb_2O_3 (400℃-800℃). Heating source, microwave power and DC bias contribute to the rapid heating process, during which, part of the Sb_2O_3 nanoparticles were reduced. An intermediate product Sb_2O_3/Sb-CSNs composite (Figure 1c) was formed. (3) The growth process of graphene shell. When the temperature reached the setting value (800℃, the growth temperature of graphene), CH_4 was introduced for graphene shell growth (lasted for 2min). Eventually, Sb_2O_3/Sb-NPs were encapsulated in graphene shells and the final product Sb_2O_3/Sb@graphene-CSNs (Figure 1d) was formed.

Figure 2 illustrates the morphology details of Sb_2O_3/Sb@graphene-CSNs. As the SEM image shown in Figure 2a and b, Sb_2O_3/Sb@graphene-CSNs presents a 3D network and porous structure like metal foam. Sb_2O_3/Sb@graphene NPs thickly anchored on CSNs (Figure 2b), 3D crisscrossed transparent pathways were formed based on the interconnected carbon sheets as marked in Figure 2c. Despite the large pores in the 3D structure, lots of nano-pores appeared on carbon sheets (Figure 2d). A nitrogen adsorption/desorption isotherm was acquired to characterize the texture of the facets of the CSNs. The isotherm exhibits type IV behavior (Fig. S4a). The sharp increase in N_2 uptake at low pressure and the hysteresis loop beginning at 0.40 P/P_0 are characteristics of meso- and micro-porous structures. The Brunauer-Emmett-Teller

(BET) specific surface area of the composite was determined to be 350 $m^2 g^{-1}$. The pore-size distribution (Fig. S4b) in the range of 0.8–110 nm was analyzed using the density functional theory (DFT) method. Considering the differential pore volume, the pore dimensions are predominantly centered at 9.2 nm and 4 nm, precisely consistent with meso-porous structures. There are small populations of pores with dimensions centered at 71 nm, corresponding to small numbers of macro-porous structures. The dynamic equilibrium growth process of the composites resulted in the formation of numerous pores on the facets of the CSNs structures.

This 3D foam like structure of Sb_2O_3/Sb@graphene-CSNs, which provided good conductivity and convenient transparent pathways for both electrons and sodiun ions, is beneficial for the application of Sb_2O_3/Sb@graphene-CSNs in SIBs.

Powder X-ray diffraction (XRD) confirmed that Sb nanoparticles coexisted with two different Sb_2O_3 crystal phases in Sb_2O_3/Sb@graphene-CSNs, corresponding to the JCPDS#35-0732, JCPDS#05-0534, JCPDS#11-0689, respectively (Figure 2e). X-ray photoelectron spectroscopy (XPS) was adopted to identify the chemical state and composition of the active material. As shown in Figure 2f, the Sb 3d3/2 peaks clearly show two antimony environments: Sb^{3+} at 540.2 eV and Sb^0 at 538 eV corresponding to Sb_2O_3 and metallic antimony, respectively. These assignments are in good agreement with the XRD results. Figure S5 shows the Raman spectrum for the as prepared composites. All peaks with Raman shifts below 1000 cm^{-1} observed in the spectrum correspond to Raman scattering of Sb_2O_3. As illustrated in the inset spectrum, the obvious peaks at 143, 191, 297cm^{-1}, characteristic of the orthorhombic Sb_2O_3, which was similar to that reported by other workers[23-25]. The other peaks in the spectrum correspond to the first- and second-order Raman scattering in the carbon materials. Two peaks at 1358 and 1601cm^{-1} are attributed to different forms of

graphite carbon[26]. The shapes and widths of the peaks indicate a poor crystallization (the existence of both amorphous and graphite carbon). The most important feature in Raman spectrum of graphene is 2D peak, and its intensity and position are widely used to estimate the number of layers in graphene samples. The small peak at 2701cm^{-1} with a small shoulder at 2665cm^{-1} appeared on the broadening convex, meaning that the laser irradiated region consisting of 3-4 layers graphene in the light of the explanation by Ferrari et al[27]. The percentage of carbon and Sb-based active material was determined by thermo gravimetric analysis (TGA) in air. As illustrated in Figure 2g, the slight weight loss around 100℃ is due to water evaporation and the dehydration condensation of carbonyl/ carboxyl on the surface of carbon sheet. The weight loss around 510℃ is mainly attributed to the oxidation of carbon, and the subsequent slow weight increase after 510℃ might be due to the oxidation of the few Sb NPs. Based on the TGA result above, the percentage of Sb_2O_3/Sb in the Sb_2O_3/Sb@graphene-CSNs composite was calculated as 65.3wt% (Sb/Sb_2O_3=1:2.75).

Transmission electron microscopy (TEM) micrographs illustrate the structure details of the composites before and after the growth of graphene/graphite. Integrate pieces of carbon sheets anchored with Sb_2O_3/Sb and Sb_2O_3/Sb@graphene nanoparticles were observed. As shown in Figure 3a,b, there is no obvious agglomeration of nanoparticles after the growth of graphene except for the rougher surface. The improved heating rate effectively prevented the aggregation of active nanopartiles. Figure 3c clearly illustrates the uniform distribution of Sb_2O_3/Sb@graphene nanoparticles on carbon nanosheet. The inset statistical result shows that the nanoparticles mainly ranged from 18nm to 22nm. High resolution TEM micrographs and their corresponding fast Fourier transform (FFT) (Figure S6) reveal fine lattice and crystalline nature of a Sb metal (Figure 3d) nanoparticle and

Sb_2O_3 (Figure 3e) nanoparticle, which is corresponding to the XRD result of Sb_2O_3/Sb-CSNs. The deposition time was controlled to obtain appropriate thick carbon shells. As shown in Figure 3f, 3-4 each nanoparticle was enwrapped graphene layers; a randomly chosen one shows orthorhombic Sb_2O_3 structure (Figure 3g). The Energy Dispersive Spectrometer (EDS) mappings of typical areas were acquired to study the distribution of Sb and Sb_2O_3 nanoparticles. As illustrated in Figure 3h, carbon and oxygen homogenously distributed in the selected area while antimony only distributed in the area where the particles existed, indicating that these nanoparticles are Sb metal. Based on the C K-edge image in Figure 3i, it was verified that the outer hollow spheres with weaker signals recorded from the center are C shells, whereas the inner particles are Sb_2O_3 cores, based on the Sb L-edge and O K-edge image.

The electrochemical performance of Sb_2O_3/Sb-CSNs was firstly tested by cyclic voltammetry at 0-2.5V and 0.1 mV/s to study the electrochemical reaction mechanism. As illustrated in Figure 4a, three cycles of the cyclic voltammograms (C-V) curve were recorded. A wide cathodic peak at 0.05-0.6 V appeared in the first reduction process, which corresponding to the formation of SEI film and Na_xSb alloys. In the following reduction reactions, the wide peak split into two sharp peaks at 0.4 V and 0.8 V associated with the reduction reaction of SbO_x ($SbO_x + 2xNa^+ + 2xe^- \rightarrow Sb + xNa_2O$)[21, 22] and the alloying of Sb with Na^+ ($2Sb + 6Na^+ + 6e^- \rightarrow 2Na_3Sb$)[11]. The positions of anodic peaks in each oxidation processes remained unchanged, as marked in Figure 4a, two peaks at 0.75V and 0.81V corresponded to dealloying reaction process ($Na_xSb \rightarrow Sb + 2xNa^+ + 2xe^-$)[28], the other wide peak at 1.3-1.7 V was ascribed to the oxidation of Sb ($Sb + 3Na_2O \rightarrow SbO_x + 2xNa^+ + 2xe^-$)[21, 22]. All the Na-storage mechanisms analyzed above were determined by *ex situ* XRD measurements of the

active materials. The electrodes were disassembled at various charging (2V, 1V)/discharged states (0.7V) during the galvanostatic charging/discharging (30 mA g^{-1}) process. As illustrated in Figure 4c, diffraction peaks from metal Sb can be found in the XRD pattern when the cell was charged to 1 V. After charging to 2 V, the main diffraction peaks moved to the same positions as that of the initial sample, except for some differences in peak intensity, indicating the recrystallization of Sb_2O_3/Sb and the content changes of each phase (Sb_2O_3, PDF#05-0534; Sb_2O_3, PDF#11-0689; Sb, PDF#35-0732). During the discharging process, weak XRD diffraction peaks from metal Sb appear again after discharging to 0.8 V. Unfortunately, there is no peak feature of Sb-Na alloy at fully discharged state (0.001V), which is due to the possibly unstable property of Sb-Na alloy in air. As a proof, the sample was test in the high vacuum TEM system, and the TEM micrograph and its corresponding selected - area electron diffraction (SAED) in Figure S8 proves the existence of Na_3Sb.

In a word, the electrochemical conversion process could be described as follows: $Sb_2O_3 + 6Na^+ + 6e^- \leftrightarrow 2Sb + 3Na_2O$, $2Sb + 6Na^+ + 6e^- \leftrightarrow 2Na_3Sb$.

Figure 4b presents the charge and discharge curves of Sb_2O_3/Sb-CSNs under a constant current density 0.1 A/g in the voltage range of 0-2 V. Clearly, the charge/discharge plateaus were consistent with the peaks in the C-V curve, which further validated the conversion mechanism. For example, in the first discharge cycle, a long discharge voltage plateau at 0.4-1.2 V corresponded to the peak at 0.05-0.6 V in the C-V curve, both of which were caused by the formation of SEI film, reduction of Sb_2O_3 and alloying of Na^+ with Sb; In the first charge cycle, three plateaus at 0.65 V, 0.7 V and around 1.3-1.5 V corresponded to the peaks at 0.75 V, 0.81 V and 1.3-1.7 V in C-V curve, respectively. The discharge and charge capacity of the first cycle was 733.6 mAh g^{-1} and 527.9 mAh g^{-1} with a Coulomb efficiency was as high as 71.9%.

The low Coulomb efficiency was mainly due to the irreversible formation of SEI film. The charging/discharging capacities for the 2nd, 200th, 275th were 522 mAh g^{-1}/525.4 mAh g^{-1}, 491 mAh g^{-1}/493 mAh g^{-1} and 486.5 mAh g^{-1}/487 mAh g^{-1}, indicating an excellent capacity retention property. The Coulomb efficiency was above 98% from the second cycle, demonstrating a stable structure of Sb_2O_3/Sb@graphene-CSNs.

The electrochemical cycling stability of the Sb_2O_3/Sb@graphene-CSNs anode was tested under galvanostatic conditions. As illustrated in Figure 4d, the composite completed more than 275 cycles under a current density of 0.1 A/g with excellent capacity retention. The desodiation capacity (C) retention rates (C_r) (C_r=$C_{in\ each\ cycle}$/C_{2nd}) were 98%, 93.4%, 92.7% for the 100th, 200th, 275th cycles, respectively. Another 55 cycles were achieved under 0.2A/g to investigate the long life of Sb_2O_3/Sb@graphene-CSNs. The electrolyte used in our experiment was EC/DMC without FEC additive. For comparison, the cycling stabilities of SIBs based on Sb_2O_3/Sb-CSNs and Sb_2O_3/Sb@graphite-CSNs were presented. As illustrated in Figure S3, without the encapsulation of carbon shell, the capacity of Sb_2O_3/Sb-CSNs degraded fast due to pulverization and exfoliation of active material caused by the large volume change during the cycling process. Meanwhile, the thickly enwrapped Sb based material (Sb_2O_3/Sb@graphite-CSNs) displayed good cycling stability but low capacity. Consequently, it is easy to associate the excellent cycle stability with the effectiveness of thin wrapped (Sb_2O_3/Sb@graphene) and well-dispersed nano-structure of Sb_2O_3/Sb@graphene-CSNs.

To verify the robust rate capability of the Sb_2O_3/Sb@graphene-CSNs anode, the Sb_2O_3/Sb@graphene-CSNs anode was cycled at various current rates from 20 mA g^{-1} to 5 Ag^{-1} in the potential range of 0.001-2 V. As shown in Figure 4e, the Sb_2O_3/Sb@graphene-CSNs anode could reach a significant desodiation capacity of

611.5 mAh g^{-1} at 20 mA g^{-1} and maintains 220.8 mAh g^{-1} even at 5 A g^{-1}. The capacity of each current density was recovered when it had reduced back to the corresponding initial current density. Good rate capacity commonly coincided with the super conductivity of electrodes. To study the electrical conductivity condition of Sb_2O_3/Sb@graphene-CSNs, we performed electrochemical impedance spectroscopy (EIS) measurements of both Sb_2O_3/Sb -CSNs and Sb_2O_3/Sb@graphene-CSNs after running a few cycles. The EIS spectra for both electrodes in Figure 4f are typically composed of an inclined line in the low-frequency region and a depressed semicircle in the high-frequency region. The inclined line corresponds to the sodium ion diffusion impedance, and the depressed semicircle mainly consists of the interfacial charge transfer impedance at the medium-to-high frequency range. The comparison of the semicircle diameter clearly indicates that the charge transfer resistance of Sb_2O_3/Sb@graphene-CSNs is significantly smaller than that for Sb_2O_3/Sb-CSNs. Meanwhile, there is no significant difference in the length of sodium ion diffusion pathways between Sb_2O_3/Sb-CSNs and Sb_2O_3/Sb@graphene-CSNs.

The outstanding electrochemical performance above was stimulation for the investigation of the conversion mechanism and structure changes of Sb_2O_3/Sb@Graphene-CSNs during the cycling process. For comparison, SIBs based on Sb_2O_3/Sb-CSNs and Sb_2O_3/Sb@graphite-CSNs were disassembled (at fully charged state 2V) and characterized by TEM after cycling at the same condition (30 mA g^{-1}, 0-2V, 10 cycles). As shown in Figure 5a, the Sb_2O_3–NP in Sb_2O_3/Sb-CSNs was about 18nm, which pulverized into a pile of smaller NPs (2.6-3nm) (Figure 5b) after cycling. As known, alloy-based materials (metal/metal oxide) were commonly hindered by their huge volume changes during charging/discharging process in practical application; the large volume change commonly caused the pulverization of

NPs, which will result in the formation of unstable SEI film and a loss of connection of active materials with current collectors (Figure 5c). This phenomenon was considered as the main reason for the unstable cycle property and capacity decay of these materials. Sb_2O_3/Sb NPs were encapsulated by the highly ordered thick graphite layer in Sb_2O_3/Sb@graphite-CSNs (Figure 5d). Therefore, the sodium ions could not pass through the graphite shell and react with Sb_2O_3/Sb cores (Figure 5e), which result in low capacity and unchanged structure (Figure 5f). In a word, neither the bare Sb_2O_3/Sb NPs nor the thickly enwrapped Sb_2O_3/Sb NPs were idea structures for the antimony-carbon based materials when applied in SIBs. A 3-4 layers graphene shell (Figure 5g) was proved to be an appropriate choice. The structure changes of Sb_2O_3/Sb@GS-CSNs in the charging/discharging process were described in Figure 5k. After the sodiation process, the Sb_2O_3/Sb core changed into a Sb-Na alloy, the diameter was increased accordingly; meanwhile, the graphene shell was gradually enlarged by the volume expansion of Sb core and eventually partly detached from the carbon sheet (but didn't exfoliate from the CSNs and remained well electrical contact with them). Additionally, a thin SEI film that was easily penetrable with Na-ions was formed in the sodiation-expanded state and remained unbroken during the following cycles, which is an important reason for the better cycle stability of Sb_2O_3/Sb@graphene-CSNs. After the desodiation process, the initial core@shell structure was well preserved and appeared to remain in good contact with the CSNs supporter. The Sb_2O_3/Sb cores pulverized into smaller particles, which were still encapsulated in the graphene shell (Figure 5h). The HRTEM image in Figure 5i demonstrated that the graphene shell structure was retained with the enlarged lattice distance (0.51nm); small, pulverized NPs with cubic Sb_2O_3 structure can be clearly observed, which was coincide with the XRD result at fully charged state (2V).

Whether the pulverization is due to the conversion reaction of Sb_2O_3 +Na↔Sb +Na_2O with its corresponding volume expansion or due to the alloying reaction was also studied. An anode was performed in the potential of 0.7-2V at 30mA/g for 10 cycles, and then was disassembled for TEM test at fully charged state 2V. As shown in the TEM micrographs in Figure S7, minor pulverization also appeared in 0.7-2V due to the conversion reaction. Thus, it can be inferred that both of the reactions, Sb_2O_3 + $6Na^+ + 6e^- \leftrightarrow 2Sb + 3Na_2O$, $2Sb + 6Na^+ + 6e^- \leftrightarrow 2Na_3Sb$, contribute to the pulverization of the particles. The low resolution TEM micrograph presents the overall situation of a single Sb_2O_3-carbon sheet composite (Figure 5j), indicating that the structural integrity of Sb_2O_3/Sb@graphene-CSNs was well-remained.

Conclusion

In this study, a novel kind of 3D Sb_2O_3/Sb@Graphene-CSNs was synthesized through a facial high yield method. The three dimensional carbon sheet networks were the skeleton of the composites and the supporters of the Sb_2O_3/Sb@Graphene core-shell structure. Sb_2O_3/Sb@Graphene nanoparticles were uniformly anchored on both sides of the carbon sheets. The composites displayed an excellent cycle stability (92.7% retained after 275 cycles), long cycle life (more than 330 cycles) and fast charge/discharge rate. The uniquely structure of the composites, which provides an ultra-thin, flexible graphene shell to accommodate changes in volume, introduces large efficient areas, good conductivity, short transportation lengths for both Na ions and electrons, contributes most to its excellent performance.

METHODS

Synthesis of Sb@graphene-CSNs. The synthesis of carbon sheets network supported Sb@GS composites was performed in a microwave plasma enhanced

chemical vapor deposition system (MPECVD). Antimony acetate ($Sb(CH_3COO)_3$) powders (99.9%, aladdin) as precursors were uniformly spread on a ceramic substrate and transformed into the chamber. Before the experiment started, the stainless steel chamber was evacuated to 5mTorr, and temperature was set to 800℃. The temperature was controlled by heater source, MW power, pressure, and gas species and was measured by a thermocouple embedded in the substrate holder. A typical synthesis procedure mainly includes three steps: (1) the decomposition of antimony acetate (150℃-400℃). Heater source is turned on; Ar/H_2 =100/5sccm is introduced into the chamber; $Sb(CH_3COO)_3$ started to effervesce with bubbles after the temperature reached 150℃; (2) Rapid heating process accompanied by the partly reduction of Sb_2O_3 (400℃-800℃). Once the temperature increases to 400℃ and the chamber pressure was stable at 40 Torr, microwave power (750 W) and DC bias (200 V) was turned on. The temperature rapidly increased to the setting value (the growth temperature of graphene). So far, the sample becomes Sb_2O_3/Sb-CSNs. (3) the growth process of graphene shell. CH_4=30sccm is mixed in the plasma; the growth of graphene shell began and lasted for 2min. Finally, the Sb_2O_3/Sb@graphene-CSNs were produced and collected by a spoon. Sb_2O_3/Sb@Graphite-CSNs was acquired by simply prolonging the deposition time of carbon source.

Material Characterizations. TEM images were taken with a microscope (FEI Tecnai G2 F30) operated at 300 kV. SEM images were recorded on an electron microscope (Quanta 400F) operated at 20 kV. XPS measurements were carried out with an ESCA Lab250 spectrometer using a twin-anode Al Kα (1,486.6 eV) X-ray source. All spectra were calibrated to the binding energy of the C 1s peak at 284.6 eV. The base pressure was approximately 3 * 10^{-7} Pa. The obtained products were characterized by XRD (Rigaku D/max-2550 V, Cu Kα radiation). The mass content

was confirmed by Thermogravimetric analysis (TGA). XRD pattern was acquired at X-Ray Diffractometer (D-MAX 2200 VPC). Raman spectrum was acquired according to the Laser Micro-Raman Spectrometer (Renishaw inVia, France), the wavelength applied was 514nm.

For post-cycling characterization of the anodes, coin cells were disassembled in an argon-filled glove box and rinsed in dimethyl carbonate. The cells were opened at a fully charged state were cycled to 2 V at a low rate (30mA g^{-1}) and held there for approximately 2h before opening to ensure that the attained state was as close to fully charged as possible. Then, the anodes were dried for XRD and TEM measurements.

Electrochemical Characterizations. The anode material was prepared by mixing 80 wt% Sb_2O_3/Sb@Ggraphene-CSNs, 10 wt% carbon black and 10 wt% Polyvinylidene Fluoride (PVDF) binder in N-methylpyrrolidone (NMP) as the solvent to form homogeneous slurry. The slurry was coated on copper foil (thickness was 50μm) and dried under vacuum at 120℃ for 10h, the mass loading of active materials (Sb2O3/Sb@graphene-CSNs) on each electrode was 1.5mg, reached 0.97 mg cm^{-2}. The copper foil with active material was cut into round shape for SIB assembly. Half-cells were assembled in an Argon-filled glove box with water and oxygen levels below 1 ppm. Sodium foil was applied as reference and counter electrodes. Celgard 2400 as the separator and 1 M NaClO4 in 1 : 1 ethylene carbonate (EC)/ dimethyl carbonate (DMC), as the electrolyte. The electrochemical performances of the half-cell, including cyclic voltammetry and electrochemical impedance spectrometry were conducted by an electrochemical workstation (Solartron 1280B). The galvanostatic charge/discharge test, cycle stability at constant current is measured by an electrochemical analyzer (HJ1001SD8, OKUTO DENKO Co.). The capacity was calculated based on the total mass of Sb2O3/Sb@graphene-CSNs.

ASSOCIATED CONTENT

Supporting Information

Additional characterizations. This material is available free of charge via the Internet.

AUTHOR INFORMATION

Corresponding Authors

* E-mail: wchengx@mail.sysu.edu.cn

Notes

The authors declare no competing financial interest.

Acknowledgements

This work was financially supported by the National Nature Science Foundation of China (51125008, 11274392, U1401241).

References

1. M. D. Slater, D. Kim, E. Lee and C. S. Johnson, *Adv. Funct. Mater.*, 2013, 23, 947-958.
2. V. Palomares, P. Serras, I. Villaluenga, K. B. Hueso, J. Carretero-Gonzalez and T. Rojo, *Energ. Environ. Sci.*, 2012, 5, 5884-5901.
3. M. S. Dresselhaus and I. L. Thomas, *Nature*, 2001, 414, 332-337.
4. S. W. Kim, D. H. Seo, X. H. Ma, G. Ceder and K. Kang, *Adv. Energy Mater.*, 2012, 2, 710-721.
5. H. L. Pan, Y. S. Hu and L. Q. Chen, *Energ. Environ. Sci.*, 2013, 6, 2338-2360.
6. S. Y. Hong, Y. Kim, Y. Park, A. Choi, N. S. Choi and K. T. Lee, *Energ. Environ. Sci.*, 2013, 6, 2067-2081.
7. H. L. Zhu, Z. Jia, Y. C. Chen, N. Weadock, J. Y. Wan, O. Vaaland, X. G. Han, T. Li and L. B. Hu, *Nano Lett*, 2013, 13, 3093-3100.
8. M. Dahbi, N. Yabuuchi, K. Kubota, K. Tokiwa and S. Komaba, *Phys. Chem. Chem. Phys.*, 2014, 16, 15007-15028.
9. S. P. Ong, V. L. Chevrier, G. Hautier, A. Jain, C. Moore, S. Kim, X. H. Ma and G. Ceder, *Energ. Environ. Sci.*, 2011, 4, 3680-3688.
10. X. G. Han, Y. Liu, Z. Jia, Y. C. Chen, J. Y. Wan, N. Weadock, K. J. Gaskell, T. Li and L. B. Hu, *Nano Lett*, 2014, 14, 139-147.
11. Y. J. Zhu, X. G. Han, Y. H. Xu, Y. H. Liu, S. Y. Zheng, K. Xu, L. B. Hu and C. S. Wang, *ACS Nano*, 2013, 7, 6378-6386.
12. M. He, K. Kraychyk, M. Walter and M. V. Kovalenko, *Nano Lett*, 2014, 14, 1255-1262.
13. A. Darwiche, C. Marino, M. T. Sougrati, B. Fraisse, L. Stievano and L. Monconduit, *J. Am. Chem. Soc.*, 2013, 135, 10179-10179.
14. Y. N. Ko and Y. C. Kang, *Chem. Commun.*, 2014, 50, 12322-12324.
15. X. S. Zhou, Z. H. Dai, J. C. Bao and Y. G. Guo, *J. Mater. Chem. A*, 2013, 1, 13727-13731.
16. Y. D. Zhang, J. Xie, T. J. Zhu, G. S. Cao, X. B. Zhao and S. C. Zhang, *J. Power Sources*, 2014, 247, 204-212.
17. Y. L. Cao, L. F. Xiao, M. L. Sushko, W. Wang, B. Schwenzer, J. Xiao, Z. M. Nie, L. V. Saraf, Z. G. Yang and J. Liu, *Nano Lett*, 2012, 12, 3783-3787.
18. L. Baggetto, E. Allcorn, R. R. Unocic, A. Manthiram and G. M. Veith, *J. Mater. Chem. A*, 2013, 1, 11163-11169.
19. L. F. Xiao, Y. L. Cao, J. Xiao, W. Wang, L. Kovarik, Z. M. Nie and J. Liu, *Chem. Commun.*, 2012, 48, 3321-3323.
20. D. H. Nam, K. S. Hong, S. J. Lim and H. S. Kwon, *J. Power Sources*, 2014, 247, 423-427.
21. K. F. Li, H. Liu and G. X. Wang, *Arab. J. Sci. Eng.*, 2014, 39, 6589-6593.
22. Q. Sun, Q. Q. Ren, H. Li and Z. W. Fu, *Electrochem. Commun.*, 2011, 13, 1462-1464.
23. Z. T. Deng, F. Q. Tang, D. Chen, X. W. Meng, L. Cao and B. S. Zou, *J. Phys. Chem. B*, 2006, 110, 18225-18230.
24. S. J. Gilliam, J. O. Jensen, A. Banerjee, D. Zeroka, S. J. Kirkby and C. N.

Merrow, *Spectrochim. Acta A*, 2004, 60, 425-434.
25. G. Mestl, P. Ruiz, H. Knozinger and B. Delmon, 1994, 98, 11276-11282.
26. J. A. Yang, J. T. Chen, S. X. Yu, X. B. Yan and Q. J. Xue, *Carbon*, 2010, 48, 2665-2668.
27. A. C. Ferrari, J. C. Meyer, V. Scardaci, C. Casiraghi, M. Lazzeri, F. Mauri, S. Piscanec, D. Jiang, K. S. Novoselov, S. Roth and A. K. Geim, *Phys. Rev. Lett.*, 2006, 97.
28. A. Darwiche, C. Marino, M. T. Sougrati, B. Fraisse, L. Stievano and L. Monconduit, *J. Am. Chem. Soc.*, 2012, 134, 20805-20811.

Figure Caption

Figure 1. Schematic for the synthesis procedure of Sb_2O_3/Sb@graphene-CSNs (a-d). (e,f) were SEM micrographs of Sb_2O_3/Sb-CSNs and Sb_2O_3/Sb@graphene-CSNs corresponding to (c,d).

Figure 2. Low and high resolution SEM micrographs of Sb_2O_3/Sb@graphene-CSNs (a,b). (c) Electron and ion transport pathways marked in red lines on a high resolution SEM micrographs of Sb_2O_3/Sb@graphene-CSNs. (d) Nanopores on carbon sheet marked in red circles on a high resolution SEM micrographs of Sb_2O_3/Sb@graphene-CSNs. XRD pattern (e) and XPS spectrum (f) of Sb_2O_3/Sb@graphene-CSNs. (g) Thermogravimetric analysis (TGA) of the Sb_2O_3/Sb@graphene-CSNs active material in air.

Figure3. TEM micrographs of Sb_2O_3/Sb–CSNs (a) and Sb_2O_3/Sb@graphene-CSNs(b); (c) TEM micrographs about the Sb_2O_3/Sb distribution condition on a sheet of Sb_2O_3/Sb@graphene-CSNs . The inset in (c) was histogram statistics the dismeters of Sb_2O_3/Sb nanoparticles. (d,e) High resolution TEM micrographs of Sb_2O_3 nanoparticles on the center and edge area of a carbon sheet of Sb_2O_3/Sb–CSNs, the edge of amorphous carbon sheet could be seen clearly. (f) Encapsulated nanoparticles of Sb_2O_3/Sb@graphene-CSNs, the diameters of nanoparticles were measured and presented. (g) High resolution TEM micrographs of a single encapsulated Sb_2O_3 particle. EDS mapping of a few Sb particles (h) and one Sb_2O_3 particle (i).

Figure 4. Electrochemical conversion mechanism and electrochemical l performance of the Sb2O3/Sb@graphene-CSNs electrode as SIB anodes. (a) C-V curve of the Sb2O3/Sb@graphene-CSNs anode between 0 and 2 V at a scanning rate of 0.1 mV/s.

(b) Galvanostatic charge/discharge voltage profiles of Sb2O3/Sb@graphene-CSNs under 0.1 A/g. (c) XRD pattern recorded at different charge/discharge states. (d) Cycle performance of Sb2O3/Sb@graphene-CSNs anode at a current density of 0.1 A/g. (e) Charge/discharge capacity of the Sb2O3/Sb@graphene-CSNs anode cycled at various current densities.

Figure 5. TEM micrographs of a nanoparticle of Sb_2O_3–CSNs before (a) and after (b) the sodiation/desodiation process. (c) A Schematic for the sodiation/desodiation mechanism of (a,b). TEM micrographs of an encapsulated nanoparticle of Sb_2O_3/Sb@graphite–CSNs before (d) and after (e) the cycling process. (f) A Schematic for the sodiation/desodiation mechanism of (d,e). TEM micrographs of an encapsulated nanoparticle of Sb_2O_3/Sb@graphene–CSNs before (g) and after (h) the cycling process. (i) High resolution TEM micrograph of the endge area of (i). (j) An integrate sheet of Sb_2O_3/Sb@graphene–CSNs post cycling. (f) A Schematic for the sodiation/desodiation mechanism of (d,e).

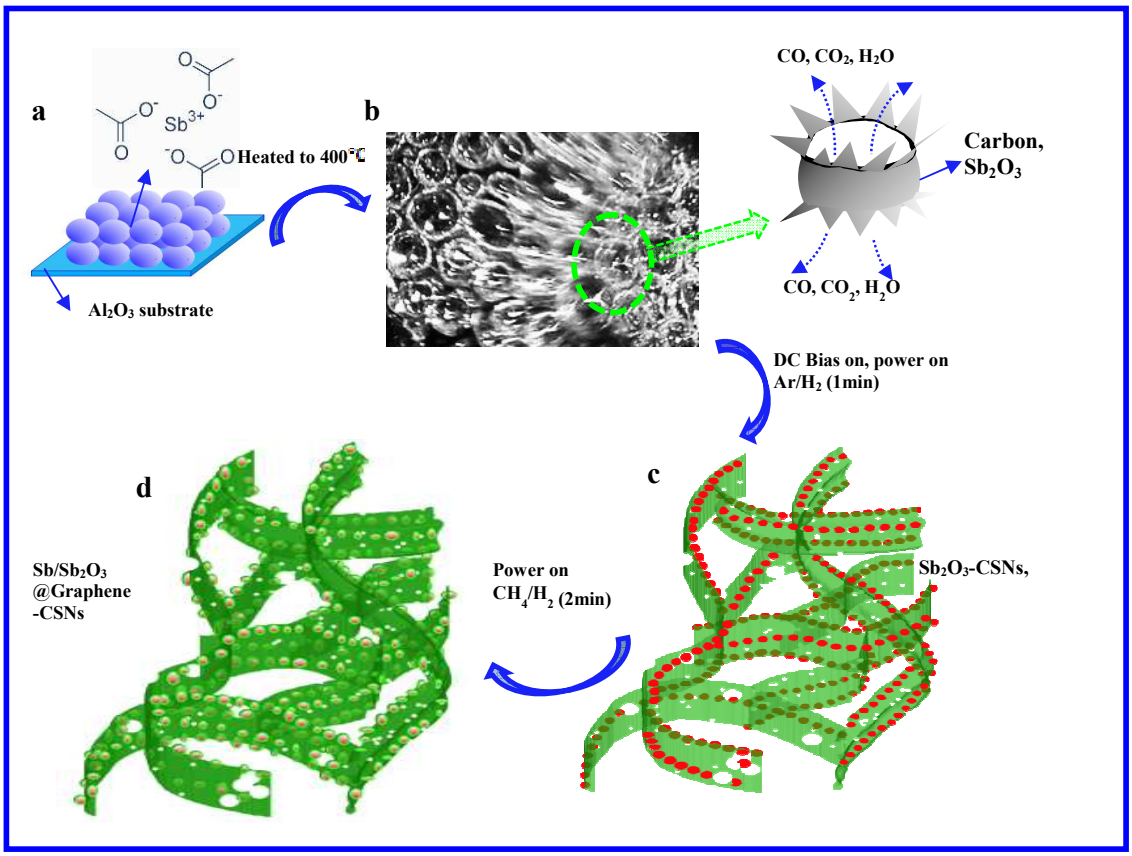

Figure 1

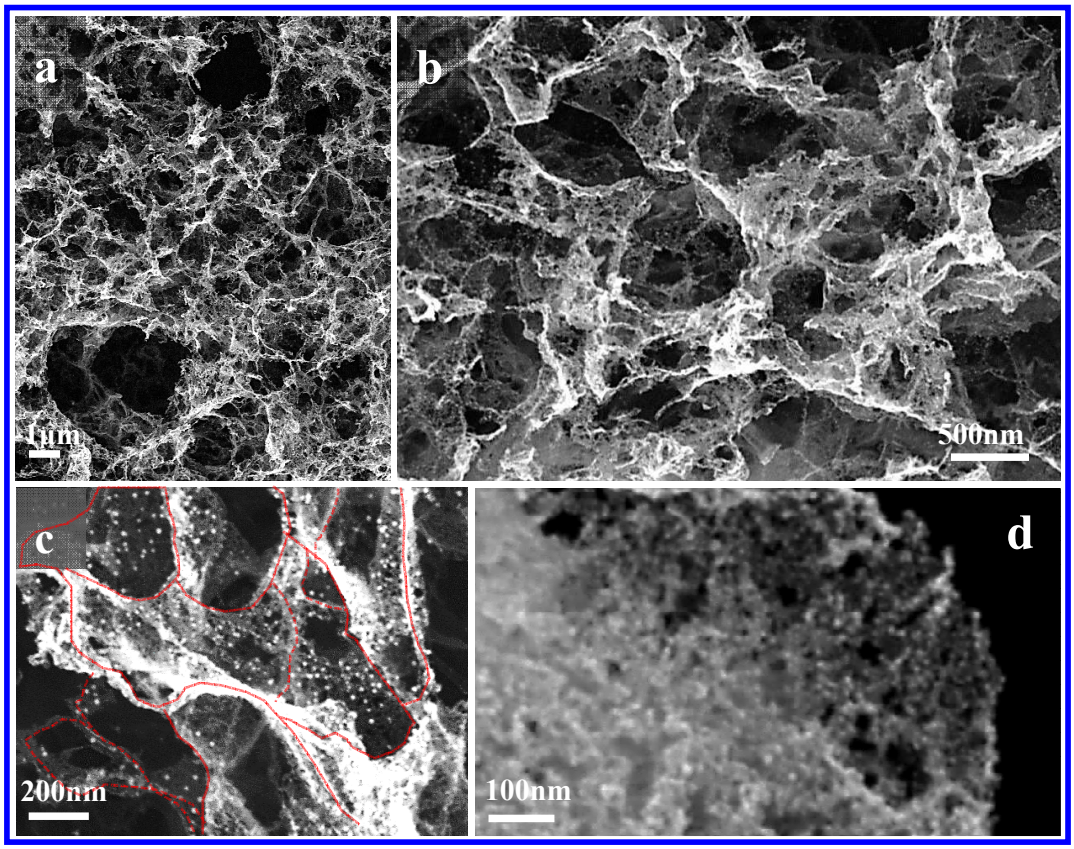

Figure 2

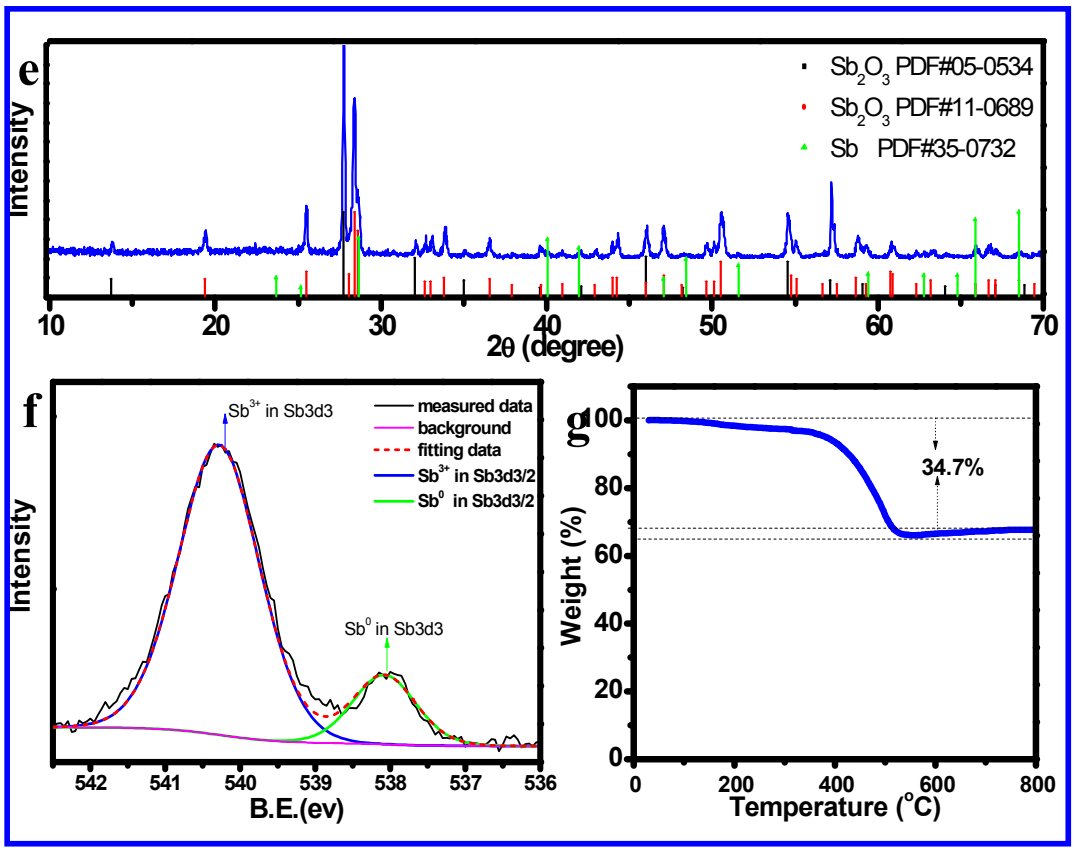

Figure 2

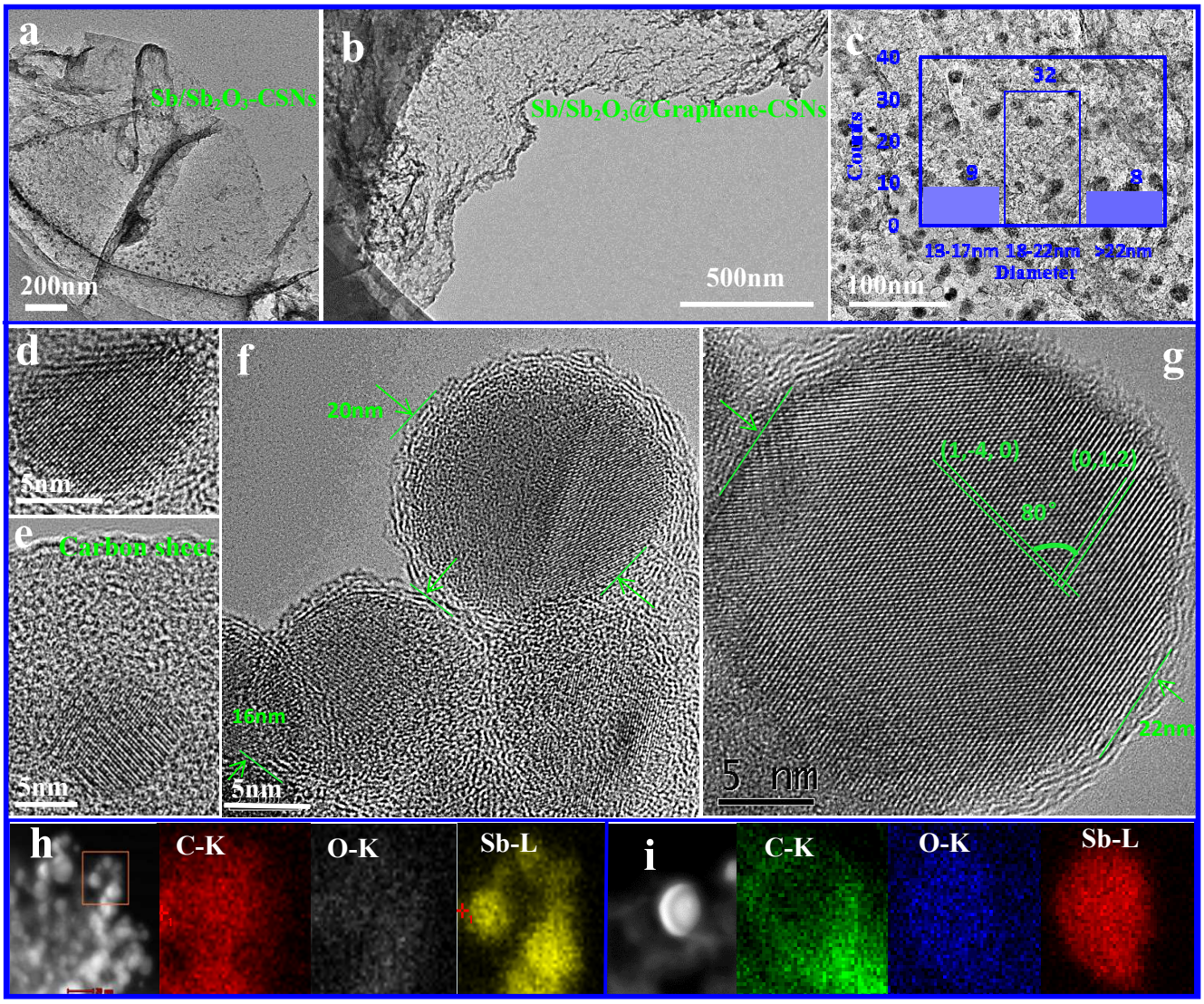

Figure 3

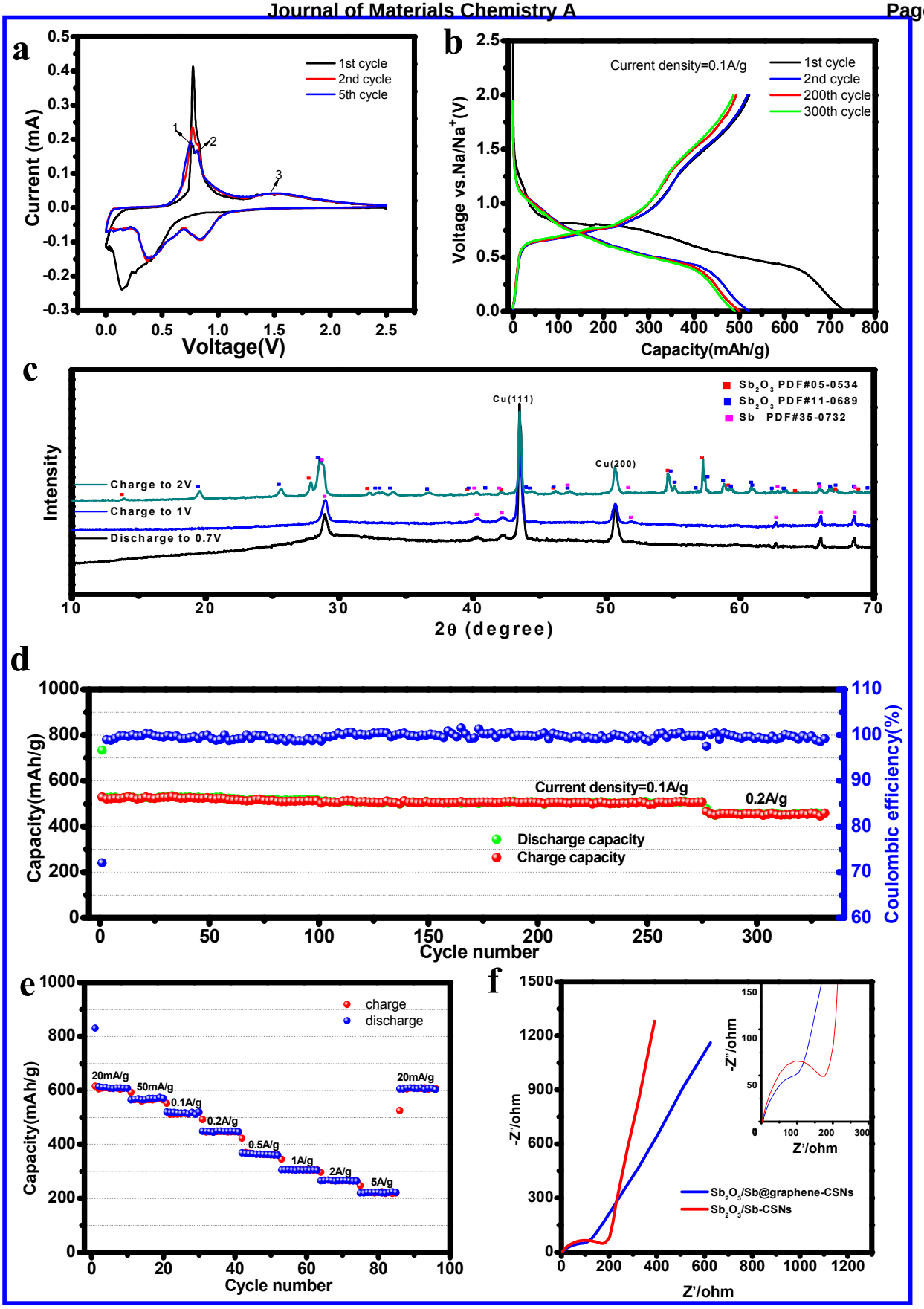

Figure 4

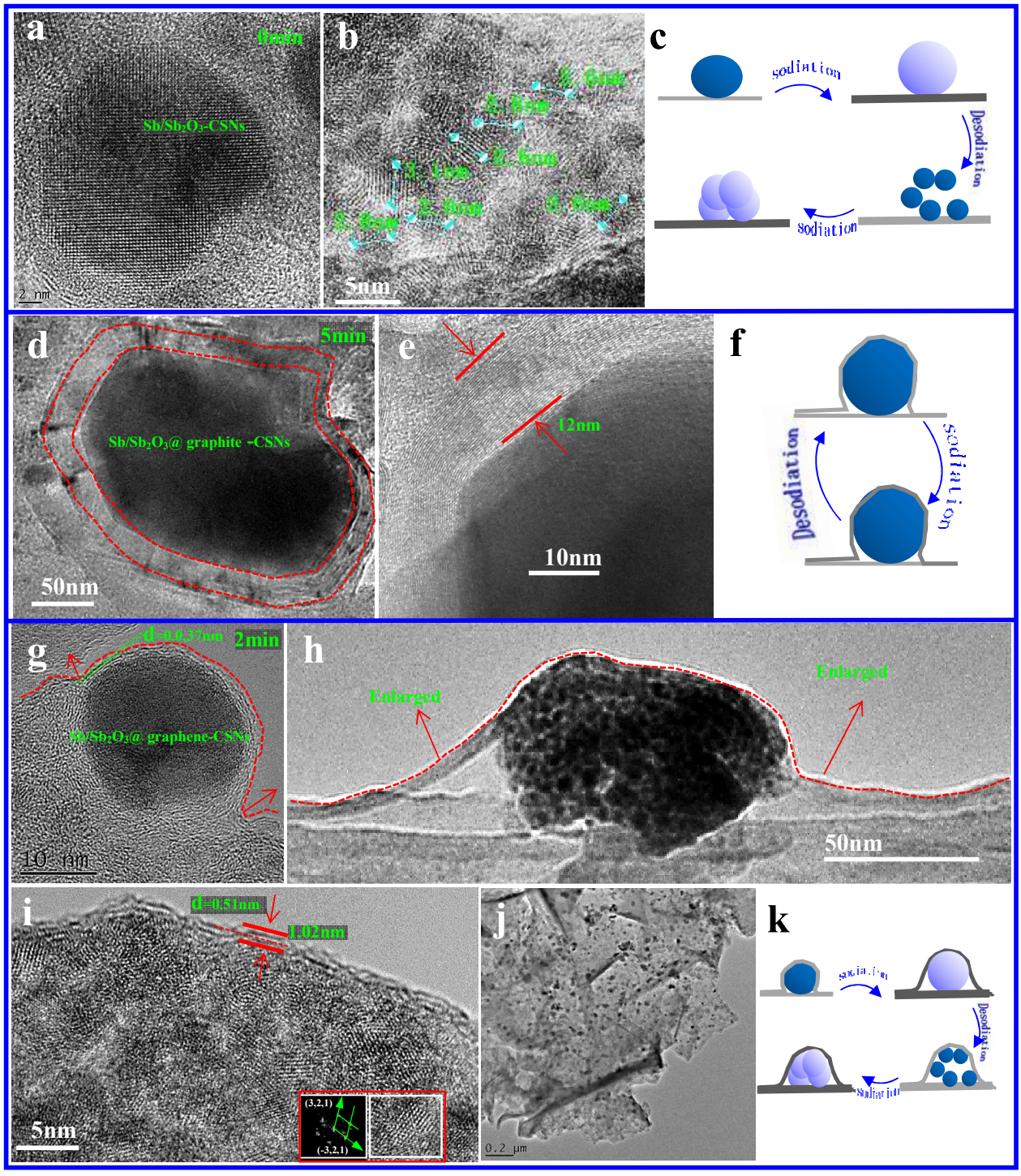

Figure 5